

## PAPER

View Article Online  
View Journal | View Issue



Cite this: *Energy Environ. Sci.*,  
2025, **18**, 6085

# Rapid electrothermal rejuvenation of spent lithium cobalt oxide cathode†

Yi Cheng,<sup>a</sup> Jinhang Chen,<sup>a</sup> Weiyin Chen,<sup>a</sup> Qiming Liu,<sup>a</sup> Obinna E. Onah,<sup>c</sup> Zicheng Wang,<sup>a</sup> Gang Wu,<sup>d</sup> Tianyou Xie,<sup>e</sup> Lucas Eddy,<sup>ac</sup> Boris I. Yakobson,<sup>ace</sup> Ju Li,<sup>b</sup> Yufeng Zhao<sup>\*ef</sup> and James M. Tour<sup>id \*aceg</sup>

Increasing use of lithium-ion batteries has triggered intensive attention to the management of end-of-life batteries. Sustainable recycling of high-value cathode materials is needed to address resource depletion and environmental challenges. Traditional battery recycling methods, including pyro- and hydro-metallurgical methods, are material-destructive processes with substantial time, energy, and chemical consumption. Here, we develop a rapid and effective electrothermal method to rejuvenate spent lithium cobalt oxide cathodes within 30 s. By incorporating Mg and Al for surface engineering during the process, the structural stability of the regenerated cathode is enhanced by mitigating detrimental phase transformations at high voltage. Thus, the upcycled cathode exhibits a high capacity of  $\sim 203 \text{ mA h g}^{-1}$  at 0.2C at an elevated cut-off voltage of 4.6 V, and maintains 84% of the initial capacity after 200 cycles. According to life cycle assessment and techno-economic analysis, our process exhibits significantly reduced environmental impacts with lower energy consumption, greenhouse gas emission, capital, and operating cost, and no solvent usage, making it a promising route to further upcycle other battery materials towards a circular economy.

Received 18th February 2025,  
Accepted 12th May 2025

DOI: 10.1039/d5ee00962f

rsc.li/ees

## Broader context

The global demand for clean energy and electrification is driving a surge in lithium-ion battery (LIB) deployment. However, the growing volume of end-of-life LIBs presents urgent environmental and resource challenges. Without effective recycling strategies, valuable materials, especially those in cathodes, are at risk of depletion, while improper disposal can cause long-term ecological damage. Current industrial methods rely on material-destructive processes that are energy- and chemical-intensive, and time-consuming. To address the challenge, this work presents a rapid and low-impact electrothermal rejuvenation strategy to restore spent cathodes by repairing their structural defects. When incorporated with heteroatom doping, the regenerated materials not only recover their original performance but even exceed that of commercial alternatives under demanding conditions. This approach supports a closed-loop battery lifecycle, reducing waste, conserving critical elements, and minimizing the environmental footprint of energy storage technologies.

## Introduction

The growing energy demand in portable electronics, electric vehicles, and grid storage systems is boosting the rapid development of lithium-ion batteries (LIBs).<sup>1,2</sup> It is estimated that global LIBs will provide  $> 6000 \text{ GW h}$  of energy with a market of  $\sim \$200$  billion in 2030.<sup>3,4</sup> However, the lifespan of LIBs is usually no longer than 10 years.<sup>5,6</sup> After reaching their end-of-life, the spent LIBs would not only lead to a waste of resources, but could also lead to harmful environmental contamination. Generally, more than 1 million spent LIBs have been disposed annually, but  $< 5\%$  of them are effectively recycled.<sup>7</sup> Cathode materials account for  $> 50\%$  of LIB costs because of critical metals such as lithium and cobalt.<sup>8,9</sup> Considering the scarcity of these batteries and the demand for LIB production will soon exceed limited mineral

<sup>a</sup> Department of Chemistry, Rice University, 6100 Main Street, Houston, TX, 77005, USA. E-mail: yi.cheng@rice.edu, tour@rice.edu

<sup>b</sup> Department of Materials Science and Engineering, Massachusetts Institute of Technology Cambridge, MA, 02139, USA. E-mail: liju@mit.edu

<sup>c</sup> Applied Physics Program and Smalley-Curl Institute, Rice University, 6100 Main Street, Houston, TX, 77005, USA

<sup>d</sup> Department of Internal Medicine, University of Texas McGovern Medical School, Houston, TX, 77030, USA

<sup>e</sup> Department of Materials Science and NanoEngineering, Rice University, Houston, TX, 77005, USA

<sup>f</sup> Corban University, 5000 Deer Park Drive SE, Salem, OR, 97317, USA. E-mail: YZhao@corban.edu

<sup>g</sup> NanoCarbon Center and the Rice Advanced Materials Institute, Rice University, Houston, TX, 77005, USA

† Electronic supplementary information (ESI) available. See DOI: <https://doi.org/10.1039/d5ee00962f>



sources, it is a pressing challenge to recycle cathode materials in an effective, environmentally, and economically prudent manner.

Among different cathode materials, lithium cobalt oxide (LCO) is used in >30% LIB manufacturing, especially in portable electronics, due to fast and reversible lithium intercalation into its layered structure.<sup>5,7</sup> Theoretically, LCO has an excellent specific capacity of 274 mA h g<sup>-1</sup>, but its practical capacity can only reach ~140 mA h g<sup>-1</sup> when charging to 4.2 V with ~50% lithium-ion de-intercalating at that stage.<sup>10</sup> Further enhancing the cut-off voltage would lead to an undesirable phase transition from an O3 hexagonal phase to a hybridized O1–O3 hexagonal phase (termed as H1–3 phase) due to high lithium loss, which accelerates LCO structure degradation and its performance decay.<sup>11,12</sup> To promote the capacity of LCO with improved cyclability, many attempts, including surface modification<sup>11,13,14</sup> and elemental doping,<sup>15–18</sup> have been applied to the LCO synthesis process. Metal ions, such as Mg<sup>2+</sup>, Ti<sup>4+</sup>, Ni<sup>2+</sup>, and Al<sup>3+</sup>, have been shown to function as pillars to stabilize the LCO structure with a high proportion of lithium loss.<sup>15–18</sup> However, these synthesized high-voltage LCO cathodes mainly originate from pure lithium and cobalt precursors. Effectively rejuvenating spent LCO into value-added high-voltage LCO with a low carbon footprint would be a sustainable approach to developing a circular economy.

Currently, cathode recycling methods include the destructive metallurgical approach and the non-destructive direct recycling approach. The former requires a large amount of concentrated acid and/or high temperature to destroy the spent cathode for the preparation of lithium and cobalt precursors, which often results in the generation of secondary waste streams and substantial consumption of time and energy.<sup>6,19,20</sup> Conversely, the direct recycling strategy can heal the structural and compositional defects of the spent cathode through a non-destructive solid-state sintering or aqueous relithiation process,<sup>7,20–24</sup> which provides an efficient and economical way for LCO recycling. However, prolonged calcination for hours is often needed during the traditional direct recycling process. Therefore, developing a fast and effective direct recycling method is preferred.

The electric heating technique has emerged as a feasible route for the synthesis<sup>25–30</sup> and recycling<sup>31–35</sup> of battery materials with high efficiency and low cost, which provides a potential opportunity for cathode upcycling. Here, we develop a rapid electrothermal rejuvenation (RER) method, which can rapidly regenerate the spent LCO into a high-voltage stable cathode through lithium replenishment and Mg/Al doping. This method exhibits the merits of high heating (~10<sup>3</sup> °C s<sup>-1</sup>) and cooling rates (~5 × 10<sup>2</sup> °C s<sup>-1</sup>), and short heating duration (~30 s) with low cost and environmental impacts when compared with traditional furnace heating. The regenerated LCO cathode shows a high capacity of ~203 mA h g<sup>-1</sup> at 0.2C with 84% capacity retention after 200 cycles in the potential range of 3.0–4.6 V, which demonstrates a far superior battery performance compared to the commercial LCO cathode.

## Results and discussion

### Electrothermal setup for cathode upcycling

In our design, carbon felt functioned as the electric heater, where its center part was excavated to a concave area. Typically,

with a size of ~4.0 cm × 8.0 cm × 6.3 mm and an excavated depth of 3.0 mm, the resistance of the carbon felt heater is ~0.6 Ω. Spent LCO (s-LCO) mixed with Li<sub>2</sub>CO<sub>3</sub> and MgO/Al<sub>2</sub>O<sub>3</sub> dopants were loaded onto the concave part, and another piece of carbon paper was capped onto its surface. A commercial arc welder was employed as a constant electrical power source. When the current goes through the carbon felt, it heats the reactants through thermal conduction, which has a higher heating efficiency than thermal conduction in conventional furnaces. The concave part with a smaller cross-section area and higher resistance enables the formation of a heat-localized zone, which further benefits the sample heat efficiency (Fig. 1a and Fig. S1, Note S1, ESI†). Temperature-dependent X-ray diffraction (XRD) results exhibit a distinct downshift of the (003) peak in the temperature range of 600–700 °C (Fig. 1b), which can be ascribed to the increase of LCO interlayer spacing caused by Li and Mg/Al insertion.<sup>16,22</sup> The thermogravimetric analysis (TGA) results also revealed that the decomposition of Li<sub>2</sub>CO<sub>3</sub> requires a temperature higher than 600 °C (Fig. S2, ESI†). Even though MgO and Al<sub>2</sub>O<sub>3</sub> did not show an obvious weight loss in the temperature range of 25–1000 °C (Fig. S3, ESI†), a similar shift of the (003) peak was observed at ~650 °C in the temperature-dependent XRD patterns by mixing s-LCO with MgO/Al<sub>2</sub>O<sub>3</sub> dopants (Fig. S4, ESI†). This result confirmed the Mg/Al insertion temperature is ~650 °C.

During RER process, benefitting from the continuous and stable current input (Fig. S5, ESI†), and good thermal stability of the carbon felt heater, a steady temperature at ~750 °C was maintained for 30 s with an input current of 12 A, where the temperature variation is low to ~3% with high heating (~10<sup>3</sup> °C s<sup>-1</sup>) and cooling rates (~5 × 10<sup>2</sup> °C s<sup>-1</sup>, Fig. 1c). The heating temperature can further be precisely controlled from 700–1200 °C by modulating input current and/or carbon felt size (Fig. 1d and Table S1, Fig. S6, Note S1, ESI†).

To determine the optimal heating temperature for LCO regeneration, we characterized the rejuvenated LCO (r-LCO) under different temperatures by XRD. At the heating temperature of 700 °C, Li<sub>2</sub>CO<sub>3</sub> residues were detected, indicating incomplete lithium replenishment (Fig. S7, ESI†). Upon increasing the temperature to ~750 °C, Li<sub>2</sub>CO<sub>3</sub> signals disappeared (Fig. S7b, ESI†), and a decrease in the c-lattice parameter of LCO suggested decreased interlayer spacing with lithium replenishment. However, further increasing the temperature led to the formation of CoO and Co<sub>3</sub>O<sub>4</sub> (Fig. S7c–f and Table S2, ESI†), which can be ascribed to the thermal degradation of s-LCO. Therefore, 750 °C was chosen as the optimized temperature for LCO upcycling.

### Characterizations of upcycled cathodes

After RER, the regenerated LCO with Mg/Al doping (r-LCO-MA) exhibits negligible differences in contrast and particle sizes when compared to s-LCO and commercial LCO (c-LCO, Fig. S8, ESI†). However, the impurities in s-LCO, including binder, conductive carbon, cathode electrolyte interface (CEI), and electrolyte remnants, were effectively removed with a trace amount of fluorine doping (<1 at%) on the LCO surface (Fig. S9–S13, ESI†). It is worth noting that solvent washing is not a necessary step to remove



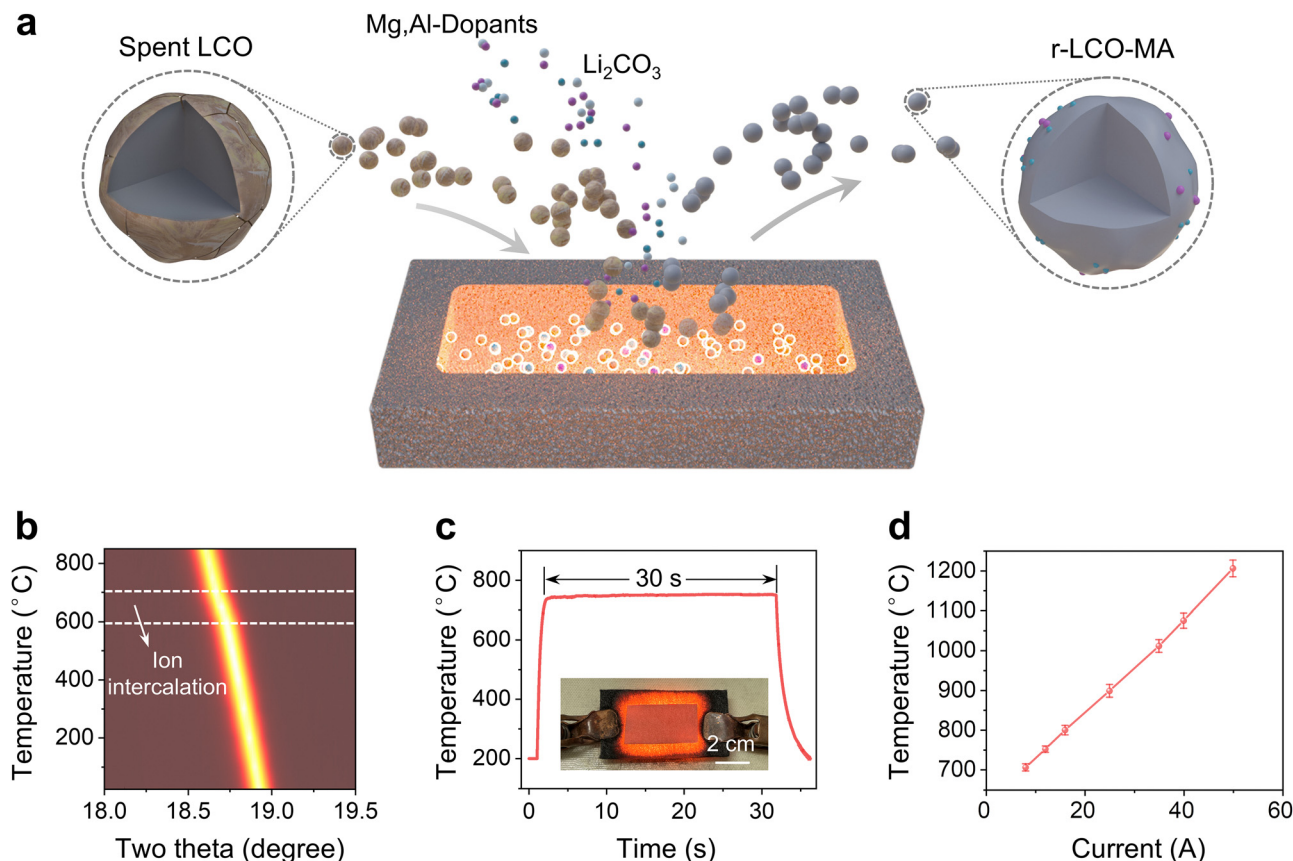


**Fig. 1** RER process for LCO cathode regeneration. (a) Schematic of the RER process. (b) Contour plot of temperature-dependent XRD pattern of spent LCO. The spent LCO was premixed with Li<sub>2</sub>CO<sub>3</sub> (15 wt%), MgO (2 wt%) and Al<sub>2</sub>O<sub>3</sub> (1 wt%). The linear peak shift can be ascribed to the thermal-induced lattice expansion, and the additional shift at 600–700 °C is related to the ion insertion into the layered structure of LCO. (c) Real-time temperature curve at a current input of 12 A for 30 s recorded by an infrared thermometer. The temperature detection range of the thermometer is 200–1500 °C. Inset: Picture of the heater during electric heating. (d) Relationship between electric heating temperature and input current. The error bars in (d) denote the standard deviation where  $N = 3$ .

impurities for cathode rejuvenation in the RER process (Fig. S14, ESI†). The agglomeration of LCO particles was released after RER (Fig. S15, ESI†), which facilitates relithiation and uniform metal doping. High-resolution transmission electron microscopy (HRTEM) images confirm the defective spinel Co<sub>3</sub>O<sub>4</sub> structure in s-LCO effectively converted into a layered structure with a high crystallinity in r-LCO-MA (Fig. 2a and b). The slight enhancement of interlayer distance is due to Mg/Al insertions. Meanwhile, the original oxygen vacancies in s-LCO were well restored (Fig. 2c), and the reduced Co<sup>2+</sup> sites in s-LCO were oxidized back to Co<sup>3+</sup> after RER (Fig. 2d). XRD patterns and Raman spectra further confirm the defect restoration after RER, and the high crystallinity of r-LCO-MA is comparable to that of c-LCO (Fig. 2e and Fig. S16, ESI†). It is worth noting that (003) peak in XRD patterns, and E<sub>g</sub> and A<sub>1g</sub> peaks in Raman spectra of r-LCO-MA exhibited a downshift, compared with those of c-LCO (Fig. S16 and S17, ESI†), indicating an increased LCO interlayer spacing. The Rietveld refinement XRD data revealed that the c-axis lattice parameter of r-LCO-MA (14.091 Å) was slightly higher than c-LCO (14.046 Å, Fig. S18 and Table S3, ESI†), indicating the increased interlayer distance due to the Mg/Al insertions.

The composition of r-LCO-MA was tested by inductively coupled plasma mass spectrometry (ICP-MS). The Li/Co mole

ratio increases from 0.77 to 0.95 after RER (Fig. 2f), indicating successful lithium replenishment. Besides, the Mg and Al concentrations in r-LCO-MA are thousands of times higher than those in s-LCO and c-LCO (Fig. S19, ESI†), demonstrating that the doped Mg/Al comes from external Mg and Al sources. By changing the ratio of MgO/Al<sub>2</sub>O<sub>3</sub> dopants with s-LCO before RER, the Mg and Al doping concentrations in r-LCO can be precisely tailored. The detailed Mg/Al doping concentrations in r-LCO-MA are listed in Table S4 (ESI†). X-ray photoelectron spectroscopy (XPS) depth analysis results exhibit that the Mg/Al are mainly distributed on the surface of r-LCO-MA with a penetration depth of 100–200 nm (Fig. S20–S22, ESI†). Scanning electron microscopy (SEM) and corresponding energy dispersive spectroscopy (EDS) mapping further confirm the uniform distribution of these doping elements on the surface of LCO particles, even with a high doping content of 9 wt% (Fig. 2g–j and Fig. S23, S24, ESI†).

### Electrochemical performance of upcycled cathode

The r-LCO-MA was applied as the cathode material for LIBs with the cut-off voltage set as 4.6 V. Firstly, we modulated the doping ratios between Mg/Al while keeping the initial input dopants concentration (MgO and/or Al<sub>2</sub>O<sub>3</sub>) as 3 wt%. The Mg/Al



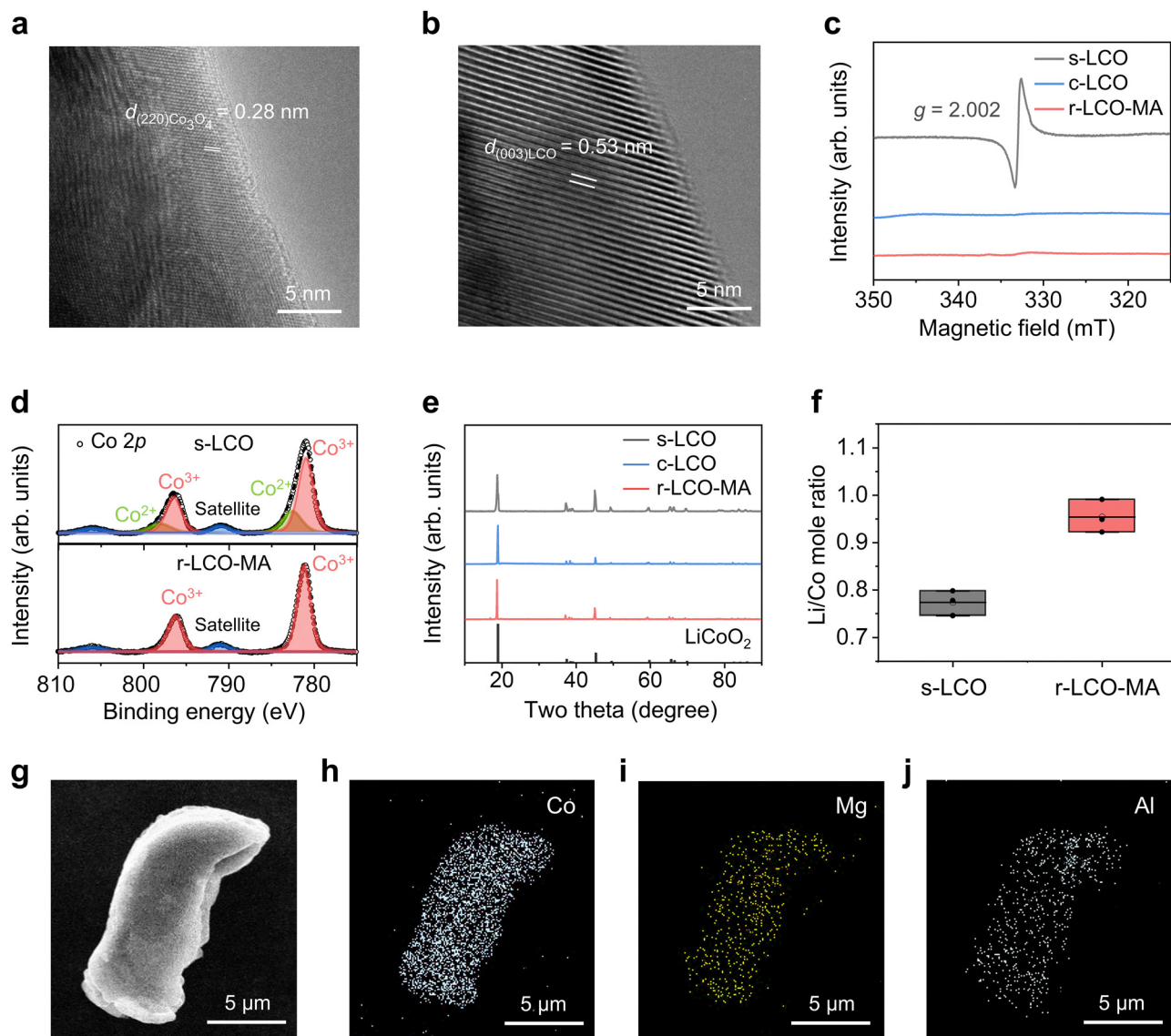


**Fig. 2** Characterizations of LCO samples. (a) and (b) High-resolution TEM images of spent LCO and r-LCO-MA. (c) EPR spectra of s-LCO (grey), c-LCO (blue), and r-LCO-MA (red). The signal with  $g$  of 2.002 corresponds to oxygen vacancy. (d) Co 2p XPS spectra of s-LCO (top), and r-LCO-MA (bottom). (e) XRD patterns of s-LCO (grey), c-LCO (blue), and r-LCO-MA (red). Powder diffraction file for  $\text{LiCoO}_2$ : 00-062-0420. (f) Mole ratio between lithium and cobalt of s-LCO (grey), and r-LCO-MA (red). (g)–(j) SEM image and corresponding element distributions of r-LCO-MA.

co-doping LCO exhibits better cycling stability than Mg or Al single-doped LCO, and the r-LCO-MA with an Mg/Al mass ratio of 2 : 1 exhibited optimal performance (Fig. S25, ESI†). Then, we changed the different doping concentrations from 0.6 wt% to 9 wt%, and found that there is a tradeoff between the battery capacity and its cycling stability, where the cathode with higher doping concentration has better stability but a decreased capacity (Fig. S26, ESI†). At high doping concentrations of 9 wt%, the r-LCO structure exhibited some distortion (Fig. S27 and S28, ESI†). Consequently, the  $\text{Li}^+$  diffusion was negatively affected (Fig. S29, ESI†). The optimal input concentration of  $\text{MgO}$  and  $\text{Al}_2\text{O}_3$  are 2 wt% and 1 wt%, respectively, defined here as r-LCO-MA.

The r-LCO-MA cathode exhibits a high capacity of  $203 \text{ mA h g}^{-1}$  at 0.2C, with 84% capacity retention after 200 cycles. On the

contrary, the c-LCO cathode lost  $\sim 96\%$  of its initial capacity after 200 cycles (Fig. 3a–c). When increasing the cycling rate, r-LCO-MA kept a high capacity of  $157 \text{ mA h g}^{-1}$  at 2C and  $127 \text{ mA h g}^{-1}$  at 4C, while the capacity of c-LCO significantly dropped to  $57 \text{ mA h g}^{-1}$  at 2C and  $8 \text{ mA h g}^{-1}$  at 4C (Fig. 3d and Fig. S30, ESI†). More importantly, when returning the cycling rate to 0.2C, the capacity of r-LCO-MA was maintained at  $195 \text{ mA h g}^{-1}$ , while the capacity of c-LCO drastically decayed to  $84 \text{ mA h g}^{-1}$  (Fig. 3d). These results indicate excellent capacity, rate performance, and high-voltage stability of the r-LCO-MA cathode. When comparing regeneration/synthesizing time and capacity retention for the reported high-voltage LCO,<sup>15,16,18,22,36–42</sup> the r-LCO-MA upcycled from RER process exhibits comparable capacity retention but a distinct shortened operating time (Fig. S31, ESI†). We further applied r-LCO-MA as



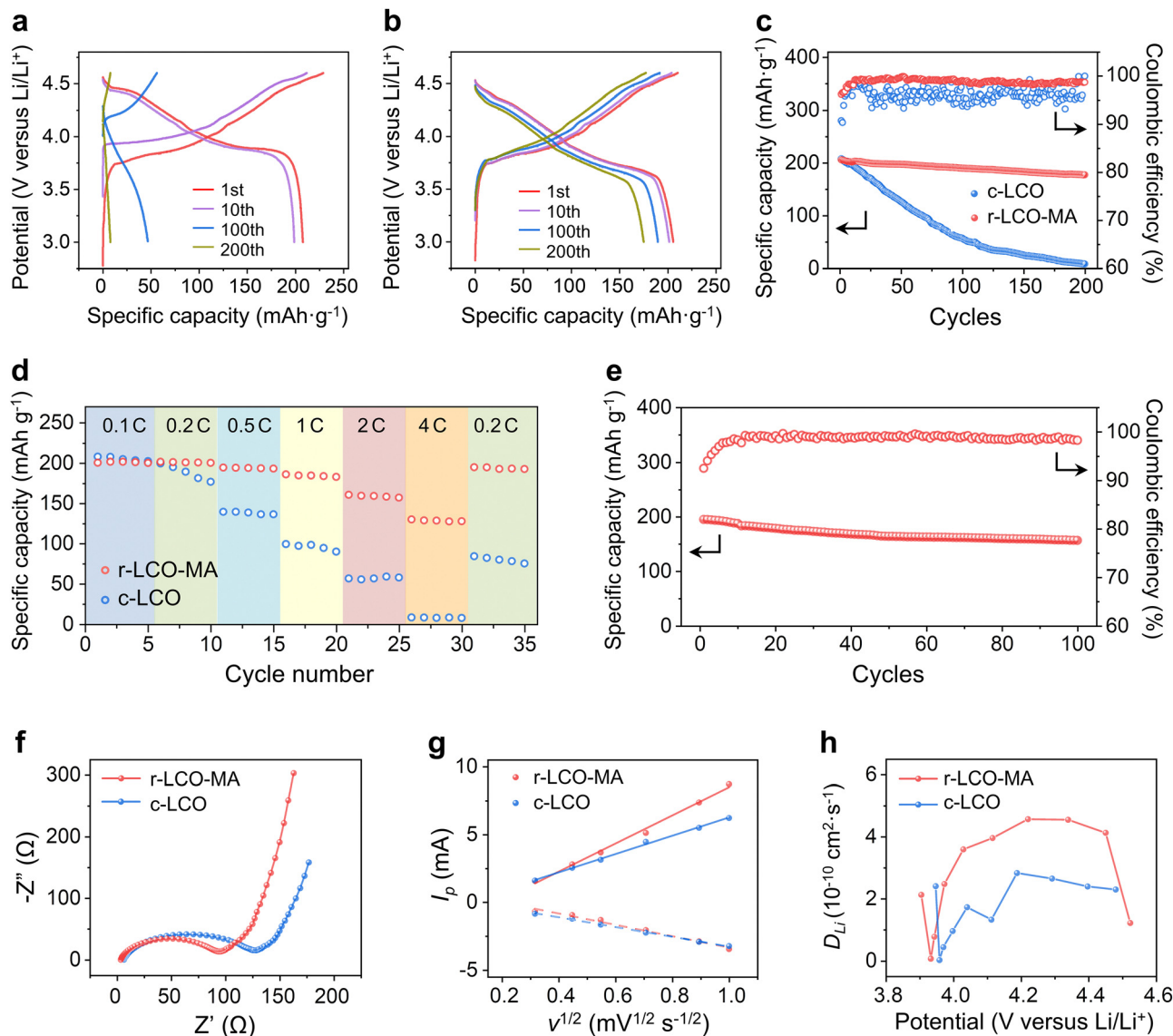


**Fig. 3** Electrochemical performance of resynthesized LCO cathode. (a) and (b) Charge–discharge profiles at different cycles for c-LCO, and r-LCO-MA. (c) Cycling stability of c-LCO (blue spot) and r-LCO-MA anode (red spot) at 0.2 C. (d) Rate capacity of c-LCO (blue spot) and r-LCO-MA anode (red spot). (e) Cycling stability of the full-cell LIB with r-LCO-MA cathode and graphite anode at 0.2 C. (f) Comparison of Li<sup>+</sup> diffusion coefficients of r-LCO-MA (red line) and c-LCO cathodes (blue line). (g) and (h) Li<sup>+</sup> diffusion coefficient of r-LCO-MA (red line) and c-LCO cathodes (blue line) during the charging and discharging process by GITT.

the cathode in a full-cell battery with commercial graphite as the anode. The full cell maintains a high capacity of 188 mA h g<sup>-1</sup> at 0.2C with a capacity retention of 80% after 100 cycles (Fig. 3e and Fig. S32, ESI<sup>†</sup>). In addition to MgO, other Mg-contained compounds, such as MgCO<sub>3</sub>, can also be used as dopants, demonstrating electrochemical performance comparable to MgO (Fig. S33 and S34, ESI<sup>†</sup>). Besides, other transition metal dopants, including Mg/Ti and Mg/Mn were also applied during the s-LCO upcycling (Fig. S35, ESI<sup>†</sup>). Both the r-LCO with Mg/Mn co-doping (r-LCO-MM) and the r-LCO with Mg/Ti co-doping (r-LCO-MT) cathodes exhibit excellent cycling stability with a capacity retention of 81% and 76%, respectively, at 0.2C after 200 cycles (Fig. S36, ESI<sup>†</sup>). Moreover, beyond LCO, this RER method was also applicable to rejuvenating spent nickel manganese cobalt oxide cathode

(s-NMC) and improved its high-voltage cycling stability (Fig. S37 and S38, ESI<sup>†</sup>). It indicates that our RER method is applicable for multiple elements doping and different cathodes to enhance their electrochemical stability after rejuvenation.

### Mechanism of cathode structural stability

To reveal the influence of Mg/Al doping for r-LCO structural stability at high voltage, Li<sup>+</sup> diffusion was characterized by cyclic voltammetry (CV, Fig. 3f and Fig. S39, S40, ESI<sup>†</sup>) and the galvanostatic intermittent titration technique (GITT, Fig. 3g and h and Fig. S41, S42 and Note S2, ESI<sup>†</sup>), respectively. The Li<sup>+</sup> diffusion coefficients in r-LCO-MA are 61% and 56% higher than those of c-LCO in charging and discharging (Fig. 3g and h, ESI<sup>†</sup>). Thirdly, we compared the morphology of r-LCO-MA cathode and

c-LCO cathode after different cycles. A continuous and stable CEI layer was formed on the surface of r-LCO-MA, while some of the c-LCO particles protruded from the CEI layer, and degraded into small particles after cycling (Fig. S43, ESI†). The thinner and more stable CEI layer in the r-LCO-MA cathode was further confirmed by O 1s XPS spectra, with a strong Co–O peak from the lattice oxygen (Fig. S44, ESI†).<sup>15</sup> The r-LCO-MA also has a higher LiF signal in F 1s XPS spectra compared with c-LCO after cycling (Fig. S45, ESI†), which comes from the CEI layer, and can reduce the electrolyte erosion and facilitate the stability of

LCO.<sup>43,44</sup> Furthermore, the LCO structure and Co valence state in r-LCO-MA remained with negligible changes after 200 cycles (Fig. S46–S48, ESI†). On the contrary, distinct Co<sub>3</sub>O<sub>4</sub> signals were observed for c-LCO in both Raman spectra and XRD patterns after 200 cycles (Fig. S46 and S47, ESI†), with a substantial ratio of Co<sup>2+</sup> in the XPS spectra (Fig. S48, ESI†).

The cycle stability of LCO is closely related to its structural evolution. Under a high voltage of 4.6 V, 80% of Li<sup>+</sup> de-intercalated from LCO, and an undesirable H1–3 phase transformation would occur with a drastic lattice contraction and

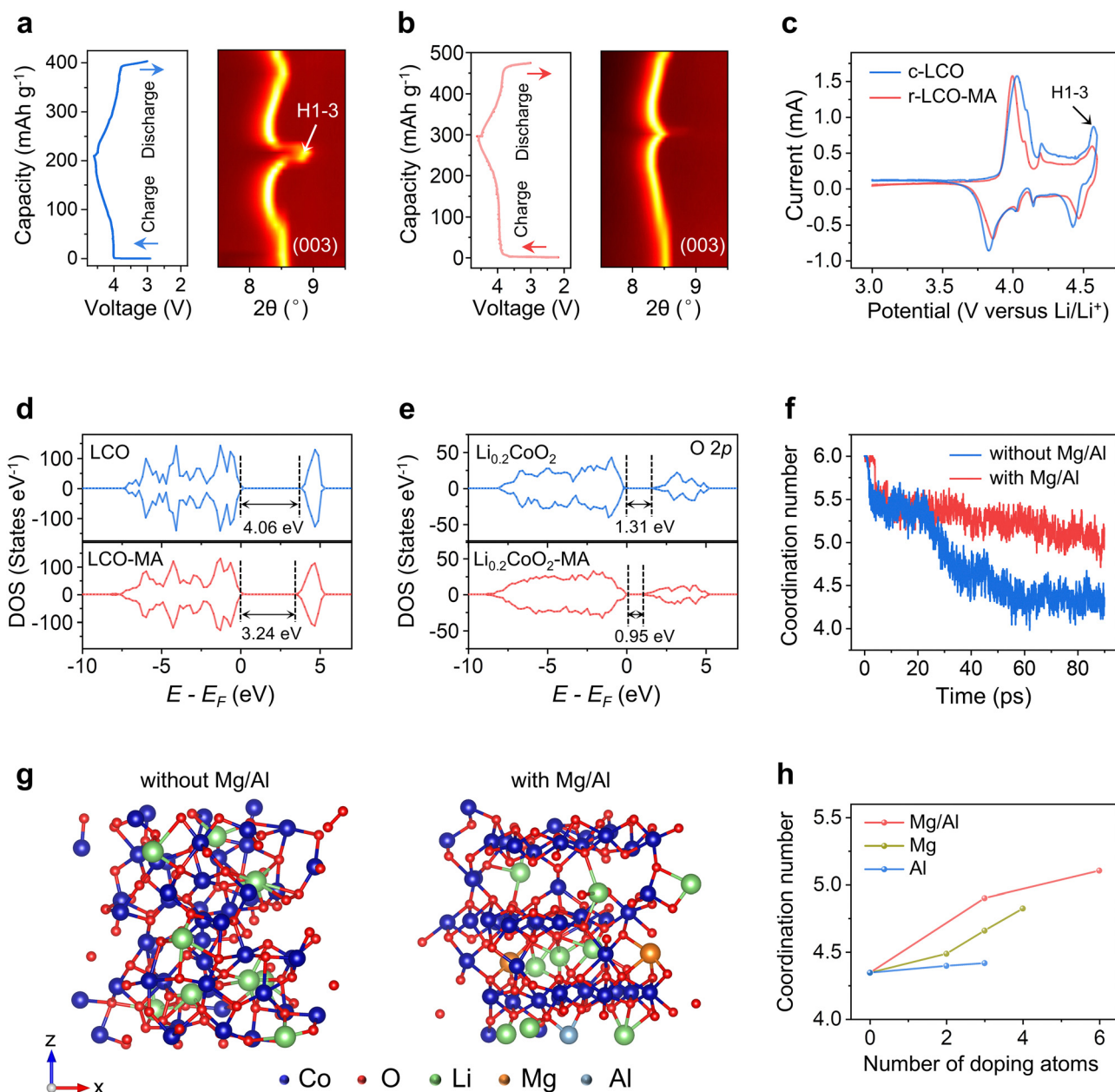


**Fig. 4** Mechanism of LCO structure stabilization by Mg/Al doping. (a) and (b) *In situ* XRD patterns of c-LCO and r-LCO-MA. (c) CV curves of c-LCO (blue line) and r-LCO-MA (red line). (d) Total DOS of LCO and LCO-MA. (e) pDOS of O 2p orbitals for Li<sub>0.2</sub>CoO<sub>2</sub> with Mg/Al (left) or without Mg/Al (right). (f) Simulated variation of Co coordination in Li<sub>0.2</sub>CoO<sub>2</sub> with Mg/Al doping (red line) or without Mg/Al doping (blue line). (g) Optimized structure snapshots of Li<sub>0.2</sub>CoO<sub>2</sub> without Mg/Al doping (left) or with Mg/Al doping (right) with the simulation time of 90 ps. (h) Relationship of Co coordination number with dopants types and their contents. Al doping (blue line), Mg doping (dark yellow line), and Mg/Al co-doping (red line).



even collapse. Thus, we conducted *in situ* XRD to investigate the phase transition behavior. The (003) peak position is related to the interlayer distance (*c*-axis lattice parameter) of the LCO lattice, which can be used as an indicator for LCO structural changes.<sup>16,45</sup> During the charging process, the (003) peak of LCO first downshifted with a lattice expansion, and then upshifted with a lattice contraction due to the Li loss. At a high voltage of 4.6 V, r-LCO-MA exhibits a relatively small upshift by 0.17° compared with c-LCO (0.57°), indicating a suppressed LCO H1–3 phase transformation after Mg/Al doping (Fig. 4a and b). The phase transition behavior was also confirmed by CV curves, with a suppressed cathodic peak related to the phase transformation at ~4.55 V for r-LCO-MA (Fig. 4c).<sup>11</sup>

To further explain the mechanism, density functional theory (DFT) and molecular dynamic (MD) simulations were employed. The simulation results revealed that doping atoms tend to occupy Li vacancies in the s-LCO with the lowest energy barrier (Fig. S49, ESI†). After Mg/Al doping, the charge density distribution of LCO is changed with a significantly reduced bandgap by

0.82 eV (Fig. 4d and e), which often leads to an improved conductivity and facilitated charge transfer, consisting with the reduced charge-transfer resistance in EIS spectra (Fig. 4f). Then, after 80% Li de-intercalation, fewer unoccupied O 2p orbitals in Li<sub>0.2</sub>CoO<sub>2</sub> with lower energy were observed after Mg/Al doping (Fig. 4g and Note S3, ESI†), indicating the reduced charge transition probability and enhanced structural stability of oxygen atoms in the LCO lattice at high voltage. The electron density distribution of Co 3d orbitals also varies after Mg/Al doping (Fig. S50, ESI†), demonstrating the different Co chemical environments in Li<sub>0.2</sub>CoO<sub>2</sub> and Li<sub>0.2</sub>CoO<sub>2</sub>-MA. The average Co coordination number was then calculated and applied as an indicator to evaluate the LCO stability after Li loss. In the initial LCO, Co<sup>3+</sup> coordinates with six O<sup>2−</sup> to form an octahedron structure, while its coordination number tends to decrease to four after phase transformation. With the Mg/Al doping, Co can keep a high coordination number after Li loss with a maintained layered structure (Fig. 4f and g). In contrast, the Co coordination number in bare LCO rapidly decreases after Li loss with a degraded structure (Fig. 4f and g).

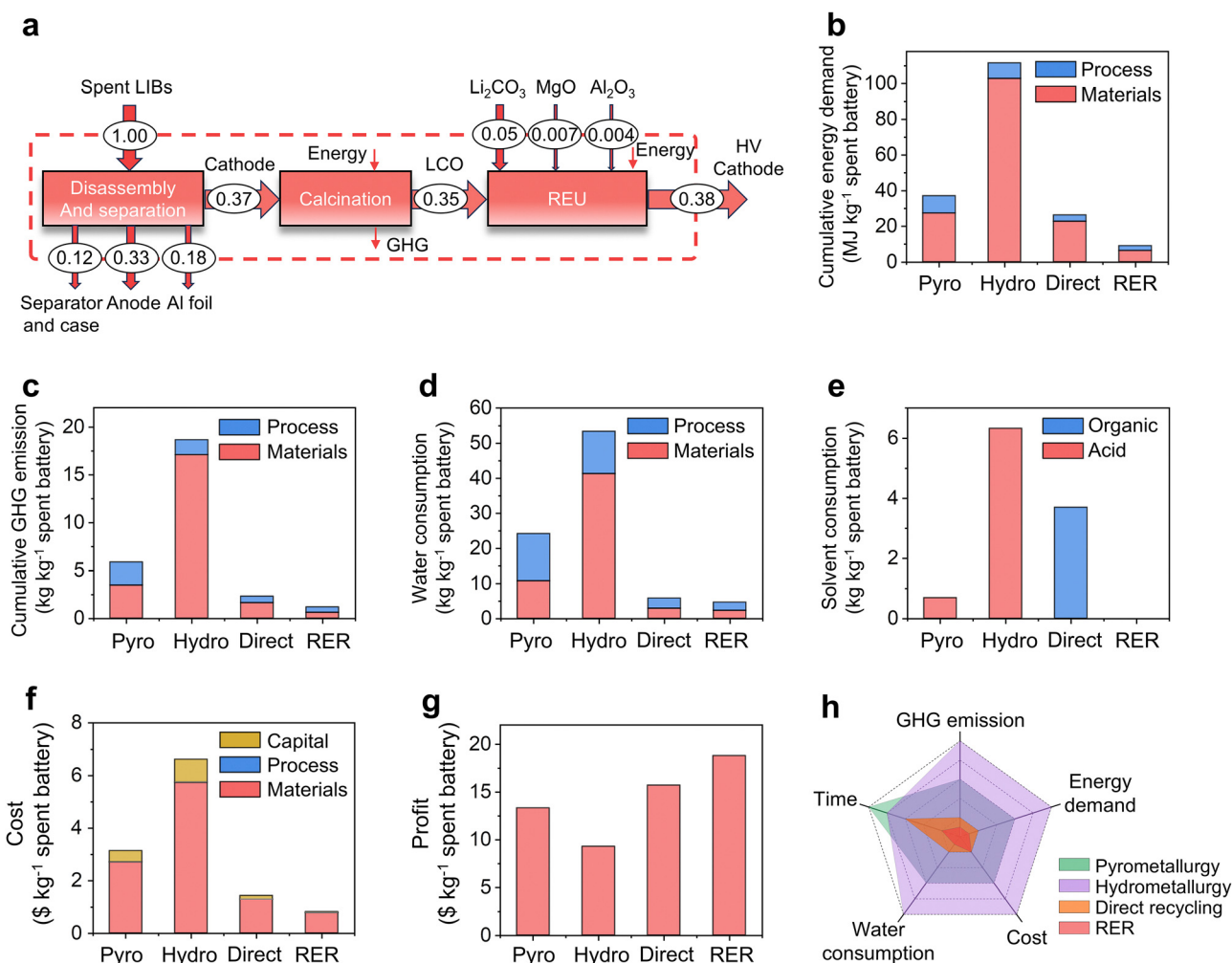


**Fig. 5** LCA and TEA assessments. (a) Materials flow of RER. The dashed rectangle denotes the system boundary. The numbers on the arrow denote the material flow mass in each step with the unit of kg. (b) Comparison of cumulative energy demand. (c) Comparison of cumulative GHG emissions. (d) Comparison of cumulative water consumption. (e) Comparison of cumulative solvent consumption. (f) Comparison of cost. (g) Comparison of profit. (h) Comprehensive comparison of different LCO recycling methods.



It was also found that Mg/Al co-doping can keep a higher Co coordination number in LCO than Mg or Al single doping with the same doping content (Fig. 4h and Fig. S51, ESI<sup>†</sup>), proving co-doping can better facilitate LCO structural stability. With the increasing doping contents, the Co coordination number approaches 6 (Fig. 4h and Fig. S51, ESI<sup>†</sup>), demonstrating that higher doping contents facilitate a higher LCO stability.

### Life cycle assessment and techno-economic analysis

To further evaluate the environmental footprints and the economic feasibility, we calculated the energy consumption of the RER process with 1.7 kW h to regenerate 1 kg of cathode (Note S4, ESI<sup>†</sup>), benefitting from the short heating duration, ultrafast heating/cooling rates, and high heating efficiency. Then, we compared our RER method with three traditional recycling processes, including hydrometallurgical, pyrometallurgical, and direct recycling by a comparative cradle-to-gate life cycle assessment (LCA) (Fig. 5a and Fig. S52, Note S5, Tables S5–S10, ESI<sup>†</sup>). The cumulative energy demand (CED) of RER is low to 9.0 MJ kg<sup>−1</sup>, which is 66% to 92% lower than other methods (Fig. 5b). RER also exhibits a 48% to 94% reduction in greenhouse gas (GHG) emission (Fig. 5c) and a 19% to 92% reduction in water consumption (Fig. 5d) without any other solvent consumption (Fig. 5e) compared to other methods. In addition, using the commercially available arc welder as the power source, the total cost to treat 1 kg of spent battery is low to \$0.87, which is reduced by 42–87% compared with other methods (Fig. 5f). It was estimated that the RER method also makes an estimated profit of \$18.8 kg<sup>−1</sup> based on the high-voltage LCO cathode (Fig. 5f and Tables S11, S12, ESI<sup>†</sup>), which is 20–102% higher than other methods. With the merits of low cost, high efficiency, zero solvent use, and excellent cathode performance (Fig. 5g), the RER process shows potential superiorities over existing cathode recycling methods, showing an encouraging environmental and economic promise for practical applications (Fig. 5h).

## Conclusions

In conclusion, we report an environmental and economical RER method to upcycle the spent LCO into a high-voltage cathode. Within a 30 s electrothermal process, the defective structure of spent LCO is restored with lithium relithiation. During this process, Mg and Al dopants diffused into LCO lattices, facilitating the cycling stability for the regenerated LCO under a high cut-off voltage of 4.6 V. With the low time- and energy consumption, low environmental impacts, and high efficiency, this process has the potential to be extended to upcycling other end-of-life battery materials. It is an attractive approach towards reducing dependence on metal mining and developing a circular battery manufacturing economy.

## Author contributions

Conceptualization: Y. C.; methodology: Y. C., J. C., W. C.; investigation: Y. C., J. C., W. C., Q. L., O. E. O., Z. W., G. W.,

T. X., and L. E.; writing – original draft: Y. C., J. C., and W. C.; writing – review & editing: Y. C., J. C., W. C., J. L., Y. Z., and J. M. T.; funding acquisition: Y. C., B. I. Y., Y. Z., J. M. T.; resources: J. L., Y. Z., B. I. Y., J. M. T.; and supervision: Y. C., J. L., Y. Z., and J. M. T.

## Data availability

The data supporting this article have been included as part of the ESI<sup>†</sup>.

## Conflicts of interest

Rice University owns intellectual property on the rapid electrothermal cathode upcycling strategy. A provisional patent was filed by Rice University, where Y. C. and J. M. T. are listed as the inventors. It has not yet been licensed. The authors declare no other competing interests.

## Acknowledgements

The authors thank Dr Bo Chen for the helpful discussion on XPS results, Dr Wenhua Guo for the assistance with TEM characterizations, Dr Jianhua Li for the temperature-dependent XRD test, and Dr Christopher Pennington for developing ICP-MS methods. The funding of the research is provided by Air Force Office of Scientific Research (FA9550-22-1-0526, J. M. T.), the U.S. Army Corps of Engineers, ERDC grant (W912HZ-21-2-0050, and W912HZ-24-2-0027, B. I. Y., Y. Z., J. M. T.), and Rice Academy Fellowship (Y. C.). Computational modeling (Y. Z. and B. I. Y.) resources were provided through allocation DMR100029 from the National Science Foundation ACCESS program. The characterization equipment used in this project is partly from the Shared Equipment Authority (SEA) at Rice University. The *in situ* XRD used in this project is from MIT.nano Characterization Facilities at Massachusetts Institute of Technology.

## Notes and references

- 1 X. Xiao, L. Wang, Y. Wu, Y. Song, Z. Chen and X. He, *Energy Environ. Sci.*, 2023, **16**, 2856–2868.
- 2 X. Yu, W. Li, V. Gupta, H. Gao, D. Tran, S. Sarwar and Z. Chen, *Global Challenge*, 2022, **6**, 2200099.
- 3 D. Song, J. Yu, M. Wang, Q. Tan, K. Liu and J. Li, *Energy Storage Mater.*, 2023, **61**, 102870.
- 4 G. Semieniuk, L. Taylor, A. Rezai and D. K. Foley, *Nat. Clim. Change*, 2021, **11**, 313–318.
- 5 E. Fan, L. Li, Z. Wang, J. Lin, Y. Huang, Y. Yao, R. Chen and F. Wu, *Chem. Rev.*, 2020, **120**, 7020–7063.
- 6 G. Harper, R. Sommerville, E. Kendrick, L. Driscoll, P. Slater, R. Stolkin, A. Walton, P. Christensen, O. Heidrich and S. Lambert, *Nature*, 2019, **575**, 75–86.
- 7 J. Wang, J. Ma, Z. Zhuang, Z. Liang, K. Jia, G. Ji, G. Zhou and H.-M. Cheng, *Chem. Rev.*, 2024, **124**, 2839–2887.
- 8 J. Baars, T. Domenech, R. Bleischwitz, H. E. Melin and O. Heidrich, *Nat. Sustainable*, 2021, **4**, 71–79.



- 9 K. Du, E. H. Ang, X. Wu and Y. Liu, *Energy Environ. Mater.*, 2022, **5**, 1012–1036.
- 10 S. Kalluri, M. Yoon, M. Jo, S. Park, S. Myeong, J. Kim, S. X. Dou, Z. Guo and J. Cho, *Adv. Energy Mater.*, 2017, **7**, 1601507.
- 11 J. Qian, L. Liu, J. Yang, S. Li, X. Wang, H. L. Zhuang and Y. Lu, *Nat. Commun.*, 2018, **9**, 4918.
- 12 J. Li, C. Lin, M. Weng, Y. Qiu, P. Chen, K. Yang, W. Huang, Y. Hong, J. Li, M. Zhang, C. Dong, W. Zhao, Z. Xu, X. Wang, K. Xu, J. Sun and F. Pan, *Nat. Nanotechnol.*, 2021, **16**, 599–605.
- 13 T. Fan, W. Kai, V. K. Harika, C. Liu, A. Nimkar, N. Leifer, S. Maiti, J. Grinblat, M. N. Tsubery and X. Liu, *Adv. Funct. Mater.*, 2022, **32**, 2204972.
- 14 J. Yao, Y. Li, T. Xiong, Y. Fan, L. Zhao, X. Cheng, Y. Tian, L. Li, Y. Li, W. Zhang, P. Yu, P. Guo, Z. Yang, J. Peng, L. Xue, J. Wang, Z. Li, M. Xie, H. Liu and S. Dou, *Angew. Chem., Int. Ed.*, 2024, **136**, e202407898.
- 15 J.-N. Zhang, Q. Li, C. Ouyang, X. Yu, M. Ge, X. Huang, E. Hu, C. Ma, S. Li and R. Xiao, *Nat. Energy*, 2019, **4**, 594–603.
- 16 Y. Huang, Y. Zhu, H. Fu, M. Ou, C. Hu, S. Yu, Z. Hu, C. T. Chen, G. Jiang, H. Gu, H. Lin, W. Luo and Y. Huang, *Angew. Chem., Int. Ed.*, 2021, **60**, 4682–4688.
- 17 N. Qin, Q. Gan, Z. Zhuang, Y. Wang, Y. Li, Z. Li, I. Hussain, C. Zeng, G. Liu and Y. Bai, *Adv. Energy Mater.*, 2022, **12**, 2201549.
- 18 M. Yoon, Y. Dong, Y. Yoo, S. Myeong, J. Hwang, J. Kim, S.-H. Choi, J. Sung, S. J. Kang, J. Li and J. Cho, *Adv. Funct. Mater.*, 2020, **30**, 1907903.
- 19 L. Yu, Y. Bai, R. Esschli, A. Bisht and I. Belharouak, *Energy Storage Mater.*, 2023, **63**, 103025.
- 20 W. Lv, Z. Wang, H. Cao, Y. Sun, Y. Zhang and Z. Sun, *ACS Sustainable Chem. Eng.*, 2018, **6**, 1504–1521.
- 21 Y. Guo, C. Guo, P. Huang, Q. Han, F. Wang, H. Zhang, H. Liu, Y.-C. Cao, Y. Yao and Y. Huang, *eScience*, 2023, **3**, 100091.
- 22 J. Wang, K. Jia, J. Ma, Z. Liang, Z. Zhuang, Y. Zhao, B. Li, G. Zhou and H.-M. Cheng, *Nat. Sustainable*, 2023, **6**, 797–805.
- 23 P. Xu, D. H. Tan, B. Jiao, H. Gao, X. Yu and Z. Chen, *Adv. Funct. Mater.*, 2023, **33**, 2213168.
- 24 Y. Liu, B. Jiao, X. Guo, S. Li, X. Lou, F. Jiang, X. Weng, M. Cao, J. Chen, Q. Zhang, G. Wang, J. Di and P. Xu, *Energy Storage Mater.*, 2024, **72**, 103684.
- 25 W. Zhu, J. Zhang, J. Luo, C. Zeng, H. Su, J. Zhang, R. Liu, E. Hu, Y. Liu, W.-D. Liu, Y. Chen, W. Hu and Y. Xu, *Adv. Mater.*, 2023, **35**, 2208974.
- 26 C. Wang, W. Ping, Q. Bai, H. Cui, R. Hensleigh, R. Wang, A. H. Brozena, Z. Xu, J. Dai, Y. Pei, C. Zheng, G. Pastel, J. Gao, X. Wang, H. Wang, J.-C. Zhao, B. Yang, X. Zheng, J. Luo, Y. Mo, B. Dunn and L. Hu, *Science*, 2020, **368**, 521–526.
- 27 Y. Cheng, J. Chen, B. Deng, W. Chen, K. J. Silva, L. Eddy, G. Wu, Y. Chen, B. Li, C. Kittrell, S. Xu, T. Si, A. A. Martí, B. I. Yakobson, Y. Zhao and J. M. Tour, *Nat. Sustainable*, 2024, **7**, 452–462.
- 28 L. Wang, S. Zhu, Z. Huang, M. Li, Y. Zhao, G. Han, Y. Li and J. Ni, *Adv. Funct. Mater.*, 2024, **27**, 2401548.
- 29 J. Luo, J. Zhang, Z. Guo, Z. Liu, C. Wang, H. Jiang, J. Zhang, L. Fan, H. Zhu, Y. Xu, R. Liu, J. Ding, Y. Chen and W. Hu, *Adv. Mater.*, 2024, **36**, 2405956.
- 30 W. Zhu, H. Su, P. Bai, Z. Li, J. Zhang, J. Zhang, M. Li, Y. Chen and Y. Xu, *Chem. Eng. J.*, 2024, **480**, 148045.
- 31 Y.-C. Yin, C. Li, X. Hu, D. Zuo, L. Yang, L. Zhou, J. Yang and J. Wan, *ACS Energy Lett.*, 2023, **8**, 3005–3012.
- 32 Y. Ji, H. Zhang, D. Yang, Y. Pan, Z. Zhu, X. Qi, X. Pi, W. Du, Z. Cheng, Y. Yao, L. Qie and Y. Huang, *Adv. Mater.*, 2024, **36**, 2312548.
- 33 T. Li, L. Tao, L. Xu, T. Meng, B. C. Clifford, S. Li, X. Zhao, J. Rao, F. Lin and L. Hu, *Adv. Funct. Mater.*, 2023, **33**, 2302951.
- 34 W. Chen, J. Chen, K. V. Bets, R. V. Salvatierra, K. M. Wyss, G. Gao, C. H. Choi, B. Deng, X. Wang, J. T. Li, C. Kittrell, N. La, L. Eddy, P. Scotland, Y. Cheng, S. Xu, B. Li, M. B. Tomson, Y. Han, B. I. Yakobson and J. M. Tour, *Sci. Adv.*, 2023, **9**, eadh5131.
- 35 W. Chen, Y. Cheng, J. Chen, K. V. Bets, R. V. Salvatierra, C. Ge, J. T. Li, D. X. Luong, C. Kittrell and Z. Wang, *Nat. Commun.*, 2024, **15**, 6250.
- 36 E. Fan, J. Lin, X. Zhang, R. Chen, F. Wu and L. Li, *Small Methods*, 2021, **5**, 2100672.
- 37 Z. Fei, Y. Zhang, Q. Meng, P. Dong, J. Fei, S. Zhou and K. Kwon, *ACS Sustainable Chem. Eng.*, 2021, **9**, 11194–11203.
- 38 S. Zhou, Z. Fei, Q. Meng, P. Dong, Y. Zhang and M. Zhang, *ACS Appl. Energy Mater.*, 2021, **4**, 12677–12687.
- 39 N. Zhang, W. Deng, Z. Xu and X. Wang, *Carbon Energy*, 2023, **5**, e231.
- 40 W. Kong, J. Zhang, D. Wong, W. Yang, J. Yang, C. Schulz and X. Liu, *Angew. Chem., Int. Ed.*, 2021, **133**, 27308–27318.
- 41 Z. Wang, Z. Wang, H. Guo, W. Peng, X. Li, G. Yan and J. Wang, *J. Alloys Compd.*, 2015, **621**, 212–219.
- 42 J.-H. Shim, N.-H. Cho and S. Lee, *Electrochim. Acta*, 2017, **243**, 162–169.
- 43 X. Z. Fan, J. H. Zhang, N. Yao, J. X. Chen, X. Chen and L. Kong, *Adv. Energy Mater.*, 2024, **14**, 2303336.
- 44 M. Yi, W. Li and A. Manthiram, *Chem. Mater.*, 2022, **34**, 629–642.
- 45 W. Cheng, M. Zhao, Y. Lai, X. Wang, H. Liu, P. Xiao, G. Mo, B. Liu and Y. Liu, *Exploration*, 2024, **4**, 20230056.

